*Progress In Electromagnetics Research B, Vol. 99, 63–81, 2023*

# An Analytical Approach for Pulse Compression Favorable Digitized Frequency Modulated Thermal Wave Imaging Technique for the Quantitative Estimation of Breast Cancer

**Anshul Sharma[1], Vanita Arora[2], and Ravibabu Mulaveesala[1, *]**

**Abstract**—Among several noninvasive diagnostic modalities used for identifying and assessing breast cancer, a recently proposed digitized frequency-modulated thermal wave imaging (DFMTWI) has emerged as a widely applied active thermographic technique. DFMTWI has demonstrated its capabilities for early diagnosis and quantitative evaluation of breast cancer by exhibiting better pulse compression properties. This approach delivers better depth resolution and sensitivity than standard thermographic techniques. The current research illustrates the novel analytical model for the pulse compression favorable DFMTWI technique for the quantitative estimation of breast cancer. Using Green's function approach, an analytical model has been solved by considering the multilayer Pennes bioheat transfer equation with adiabatic boundary conditions and a constant initial condition. The conventional thermographic techniques (such as Lock-in Thermography (LT) and Pulse Thermography (PT)) are also solved with a similar approach as followed for DFMTWI. The results obtained for the proposed DFMTWI and the conventional LT and PT thermographic techniques are then compared and validated with the numerical results obtained from the numerical simulation considering the correlation coefficient as a figure of merit for early-stage breast cancer diagnosis.

## 1. INTRODUCTION

Among all cancer types, breast cancer is the most widespread cancer worldwide with around 2.1 million cases reported in 2018, and it was estimated to rise to approximately 18 million cases by 2020 [1–3]. Although females are more susceptible to breast cancer, males also tend to acquire this disease owing to less awareness and exposure to personalized examination strategies [4]. Pathologically, breast cancer predominantly arises within the inner lining of the ducts or lymph tissues of the breast and is primarily heterogeneous. Breast cancer is classified into distinct stages, i.e., benign or malignant. It is a global issue with an enormous number of cases associated with malignant tumors that originate in breast cells [2, 5–9]. Therefore, it is crucial to develop efficient, cost-effective, and noninvasively early detection methodologies, along with awareness measures, to reduce the co-morbidity rate.

Rapid screening for breast cancer has been made possible via several diagnostic methodologies classified into imaging-based techniques and molecular biology-based detection [6]. Imaging techniques provide information based on the diseased tissue location, morphology, and diagnosis based on the contrasting biochemical agents. These techniques involve ultrasonography, mammography, magnetic resonance imaging (MRI), computed tomography (CT), positron emission computed tomography (PET), etc. [6, 1–12]. However, more often, utilizing contrasting agents for tissue imaging may lead to cellular-level damage and affect the patient's physiology and usually involves impinging high-energy

---

*Received 27 October 2022, Accepted 10 March 2023, Scheduled 20 March 2023*

[*] Corresponding author: Ravibabu Mulaveesala (mulaveesala@sense.iitd.ac.in).

[1] InfraRed Imaging Laboratory (IRIL), Centre for Sensors, Instrumentation, and Cyber-Physical Systems Engineering (SeNSE), Indian Institute of Technology Delhi, Hauz Khas, New Delhi 110016, India. [2] Indian Institute of Information Technology Una, Village Saloh, Tehsil Haroli, District Una Himachal Pradesh 177209, India.

radiations for obtaining better quality and contrasted images. Furthermore, these modalities also deliver lower resolution-based images, making it cumbersome to delineate among the normal, benign, and malignant tissues during the diagnostic procedure. Patients' comfort and tissue invasiveness are delimiting factors while working with such diagnostic methodologies. Thus, an affordable, sensitive, patient-friendly, noninvasive technique for breast cancer detection is an absolute necessity instead of a consistent rise in breast cancer cases worldwide. Thermal-based imaging modalities fulfill all such requirements of being a potent diagnostic tool, principally relying on identifying the differential temperature-based mapping of the surface in a noninvasive manner [12–15]. Since cancerous tissues tend to attain an increased blood flow rate and associated temperature fluctuations [15], thermography techniques pose an excellent fit in the diagnostic modalities. Different conventional thermographic techniques have been implemented for the early diagnosis and quantitative evaluation of breast cancer such as Lock-in Thermography (LT) and Pulse Thermography (PT). But there are different drawbacks associated with these conventional techniques such as high peak power requirement for PT to obtain higher resolution and repetition of experimentation in the case of LT because of mono modulation frequency which limits overall depth resolution. Then, to conquer the limitation of these conventional techniques, the recent DFMTWI technique has been introduced, which improved overall depth resolution and the sensitivity of the test [16–25].

The current study emphasizes the recently suggested DFMTWI technique's superiority over traditional thermographic methods (PT and LT) for the early diagnosis and quantitative assessment of breast cancer. It has been illustrated by solving the analytical models using Pennes bioheat transfer equation for adiabatic boundary conditions with the constant initial condition of typical human body temperature. It has been achieved by solving the digitized frequency-modulated, mono-frequency-modulated, and pulse-modulated incident heat flux in the case of DFMTWI, LT, and PT techniques, respectively. After that, the obtained temporal thermal data for different techniques have been processed with time domain-based data processing approaches to compare their breast cancer detection capabilities by considering correlation-based data processing approaches as a figure of merit. Lastly, the analytically obtained data were validated with the numerical data from a commercially available numerical simulator such as COMSOL Multiphysics.

## 2. THEORETICAL MODELING

This section presents an analytical approach for the quantitative estimation of breast cancer by considering a three-dimensional multilayer model (Figure 2) represented by the multilayer Pennes bioheat transfer equation. It includes thermal changes that occur due to blood perfusion in each layer in the temporal thermal distribution obtained over the living tissue and represented as [26–37]:

$$\rho_i c_{\mathrm{pi}} \frac{\partial v_i(x,y,z,\tau)}{\partial \tau} = k_i \nabla^2 v_i(x,y,z,\tau) + w_{bi}\rho_b c_b (v_a - v_i(x,y,z,\tau)) + q_{mi} \tag{1}$$

where $v_i(x,y,z,\tau)$ is the temperature $(K)$ in the $i$th tissue layer at a given spatial location $x$, $y$, and $z$ at a time instant $\tau$; $k_i$ is the thermal conductivity (W/m K) of the $i$th tissue layer tissue; $v_a$ is the artery temperature; $q_{mi}$ is the metabolic heat generation rate in the $i$th tissue layer (W/m$^3$); $\rho_i$, $c_{\mathrm{pi}}$, $w_{bi}$, $\rho_b$, and $c_b$ are the $i$th tissue layer density (kg/m$^3$), specific heat capacity (J/kg K), blood perfusion rate ((ml/s)/ml), blood density (kg/m$^3$), and blood specific heat capacity (J/kg K), respectively.

The generalized three-dimensional multilayer bioheat transfer equation was analytically solved for time-dependent heat flux which propagates perpendicular to the test object surface, and its equation can be represented as [26–37]: (The incident heat flux over modeled sample surface (at $x = x_1 = 0$)):

$$q_1 = -k_1 \frac{\partial v_1(x,y,z,\tau)}{\partial x} = q_H(\tau) \tag{2}$$

where $q_1$ is the heat flux (W/m$^2$).

Over another surface $x = x_{n+1}$ adiabatic boundary condition has been imposed which can be mathematically written as:

$$\left[\frac{\partial v_n(x,y,z,\tau)}{\partial x}\right]_{x=x_{n+1}} = 0 \tag{3}$$

Initial condition (at $x = x_1, x_2, \ldots x_{n+1};\ \tau = 0$) of the modeled sample:

$$v_i\left(x, y, z, 0\right) = v_i^o \tag{4}$$

Boundary conditions between two layers of the modeled sample were considered as follows:

$$k_i \frac{\partial v_i\left(x_{i+1}, y, z, \tau\right)}{\partial x} = k_{i+1} \frac{\partial v_{i+1}\left(x_{i+1}, y, z, \tau\right)}{\partial x} \quad \text{and} \quad v_i\left(x_{i+1}, y, z, \tau\right) = v_{i+1}\left(x_{i+1}, y, z, \tau\right) \tag{5}$$

Other boundary conditions:

$$\frac{\partial v\left(x, y_1, z, \tau\right)}{\partial y} = 0; \quad \frac{\partial v\left(x, y_2, z, \tau\right)}{\partial y} = 0; \quad \frac{\partial v\left(x, y, z_1, \tau\right)}{\partial z} = 0; \quad \frac{\partial v\left(x, y, z_2, \tau\right)}{\partial z} = 0 \tag{6}$$

It is not possible to solve the Pennes bioheat transfer equation, described in Eq. (1), directly because it is a nonhomogeneous partial differential equation. So, to solve the problem, the separation of variable methodology is employed, which involves decomposing the solution into two distinct parts: the steady state condition and transient condition. Both of these parts are then solved separately [26–37].

$$v_i\left(x, y, z, \tau\right) = v_i^{ss}\left(x, y, z\right) + v_i^{tr}\left(x, y, z, \tau\right) \tag{7}$$

where $v_i(x, y, z, \tau)$ is the temperature $(K)$ in the $i$th tissue layer at a given spatial location $x$, $y$, and $z$ at a time instant $\tau$; $v_i^{ss}(x, y, z)$ is the steady state temperature $(K)$ in the $i$th tissue layer at a given spatial location $x$, $y$, and $z$ before the implementation of the heat flux; and $v_i^{tr}(x, y, z, \tau)$ is the transient temperature $(K)$ in the $i$th tissue layer at a given spatial location $x$, $y$, and $z$ after the implementation of the heat flux at a time instant $\tau$. Substituting Eq. (7) in Eq. (1) develops two sets of partial differential equations, which are homogeneous.

### 2.1. Steady-State Solution

First, the steady-state condition representing the basal state of the biological materials can be described as [26–37]:

$$\nabla^2 v_i^{ss} - \varphi_i v_i^{ss} = -\left(\varphi_i v_a + \frac{q_{mi}}{k_i}\right); \quad where; \quad \varphi_i = \left(\frac{w_{bi}\rho_b c_b}{k_i}\right) \tag{8}$$

$$\left[\frac{\partial v_1^{ss}}{\partial x}\right]_{x=x_1} = 0; \quad \left[\frac{\partial v_n^{ss}}{\partial x}\right]_{x=x_{n+1}} = 0; \quad \left[\frac{\partial v_1^{ss}}{\partial y}\right]_{y=y_1} = 0;$$

$$\left[\frac{\partial v_2^{ss}}{\partial y}\right]_{y=y_2} = 0; \quad \left[\frac{\partial v_1^{ss}}{\partial z}\right]_{z=z_1} = 0; \quad \left[\frac{\partial v_2^{ss}}{\partial z}\right]_{z=z_2} = 0 \tag{9}$$

The interfacial boundary conditions between two layers of the modeled sample can be written as [26–37]:

$$k_i \frac{\partial v_i^{ss}\left(x_{i+1}, y, z\right)}{\partial x} = k_{i+1} \frac{\partial v_{i+1}^{ss}\left(x_{i+1}, y, z\right)}{\partial x} \quad \text{and} \quad v_i^{ss}\left(x_{i+1}, y, z\right) = v_{i+1}^{ss}\left(x_{i+1}, y, z\right) \tag{10}$$

Further, Eq. (8) is solved for boundary conditions presented in Eq. (9) and Eq. (10) by Green's function approach, and the solution is obtained as [26–37]:

$$v_i^{ss} = D_i \text{Cosh}\left(\sqrt{\varphi_i} x_i\right) + E_i \text{Sinh}\left(\sqrt{\varphi_i} x_i\right) + v_a + \frac{q_{mi}}{w_{bi}\rho_b c_b} \tag{11}$$

This temperature distribution obtained in Eq. (11) for the solution of Eq. (8) is the temperature distribution inside the biological body due to the initial temperature distribution before the employed heat flux. In Eq. (11), the values of constant coefficients $D_i$ and $E_i$ are calculated by $2n$ number of linear homogeneous equations obtained from boundary conditions [26–37].

### 2.2. Transient Solutions

The transient state represents the temporal thermal distribution inside the biological body after the implementation of heat flux, and the partial differential equation for the transient heat transfer inside the biological body can be written as [26–37]:

$$\begin{gathered}\frac{\partial v_i^{tr}}{\partial t} = \alpha_i \nabla^2 v_i^{tr} - \phi_i v_i^{tr} \\ \alpha_i = \left(\frac{k_i}{\rho_i c_{\mathrm{pi}}}\right); \quad \phi_i = \left(\frac{w_{bi}\rho_b c_b}{\rho_b c_{\mathrm{pi}}}\right)\end{gathered} \tag{12}$$

where $\alpha_i$ is the $i$th tissue layer thermal diffusivity ($\mathrm{m}^2/\mathrm{s}$); $\phi_i$ is the variable associated with the blood perfusion rate; and its unit is (ml/s)/ml.

In most of the practical situations when we are studying temperature distribution over the biological bodies, the boundary conditions are often time-dependent, which can be written as:

$$\left[-k_1 \frac{\partial v_1^{tr}}{\partial x}\right]_{x=x_1=0} = q_H(t) \tag{13}$$

$$\left[\frac{\partial v_n^{tr}}{\partial x}\right]_{x=x_{n+1}} = 0 \tag{14}$$

The initial condition is as follows:

$$v_i^{tr}(x,y,z,0) = v_i^o - v_i^{ss}(x,y,z) \tag{15}$$

The other surface is considered insulated, and their boundary condition can be described as follows:

$$\left[\frac{\partial v_1^{tr}}{\partial y}\right]_{y=y_1} = 0; \quad \left[\frac{\partial v_2^{tr}}{\partial y}\right]_{y=y_2} = 0; \quad \left[\frac{\partial v_1^{tr}}{\partial z}\right]_{z=z_1} = 0; \quad \left[\frac{\partial v_2^{tr}}{\partial z}\right]_{z=z_2} = 0 \tag{16}$$

Interfacial boundary conditions:

$$k_i \frac{\partial v_i^{tr}\left(x_{i+1},y,z,\tau\right)}{\partial x} = k_{i+1}\frac{\partial v_{i+1}^{tr}\left(x_{i+1},y,z,\tau\right)}{\partial x} \quad \text{and} \quad v_i^{tr}\left(x_{i+1},y,z,\tau\right) = v_{i+1}^{tr}\left(x_{i+1},y,z,\tau\right) \tag{17}$$

The transient heat equation, as defined in Eq. (12), has been solved using Green's function approach, considering the adiabatic boundary conditions. The modeled sample surface has been illuminated by time-dependent heat flux. However, all other surfaces are considered thermally insulated. The solution for the transient heat diffusion equation given in Eq. (12) using the generalized Green's Function approach can be expressed as follows [26–37]:

$$\begin{aligned} v_i^{tr}(x,y,z,\tau) = \sum_{j=1}^{n}\Bigg\{\sum_{p=1}^{n+1}\Bigg[&\alpha_j \int_0^{\tau}\int_{y_1}^{y_2}\int_{z_1}^{z_2}\left[g_{ij}\left(x,y,z,\tau|\varepsilon,\xi,\delta,t\right)\nabla_n v_1^{tr}(\varepsilon,\xi,\delta,t)\right]_{\varepsilon=\varepsilon_p}\mathrm{d}\delta\mathrm{d}\xi\mathrm{d}t \\ &-\alpha_j \int_0^{\tau}\int_{y_1}^{y_2}\int_{z_1}^{z_2}\left[v_i^{tr}(\varepsilon,\xi,\delta,t)\nabla_n g_{ij}(x,y,z,\tau|\varepsilon,\xi,\delta,t)\right]_{\varepsilon=\varepsilon_p}\mathrm{d}\delta\mathrm{d}\xi\mathrm{d}t\Bigg] \\ &+\int_{x_j}^{x_{j+1}}\int_{y_1}^{y_2}\int_{z_1}^{z^2}\left[g_{ij}(x,y,z,\tau|\varepsilon,\xi,\delta,0)v_i^{tr}(\varepsilon,\xi,\delta,0)\right]\mathrm{d}\delta\mathrm{d}\xi\mathrm{d}\varepsilon\Bigg\} \end{aligned} \tag{18}$$

$$where\ i = 1,2,3\ldots; \quad n = \text{number of layers}$$

Substituting the initial and boundary conditions described in Eq. (13) to Eq. (17) in Eq. (18), the overall solution for transient heat distribution Eq. (12) in the biological body can be represented as [26–37]:

$$\begin{aligned} v_i^{tr}(x,y,z,\tau) =& \left\{ \alpha_1 \int\limits_0^{\tau} \int\limits_{y_1}^{y_2} \int\limits_{z_1}^{z_2} \left[ g_{i1}(x,y,z,\tau|\varepsilon,\xi,\delta,t) \frac{\partial v_1^{tr}(\varepsilon,\xi,\delta,t)}{\partial n_1} \right]_{\varepsilon=\varepsilon_1=0} \mathrm{d}\delta \mathrm{d}\xi \mathrm{d}t \right. \\ & \left. + \sum_{j=1}^{n} \left( \int\limits_{x_j}^{x_{j+1}} \int\limits_{y_1}^{y_2} \int\limits_{z_1}^{z_2} g_{ij}(x,y,z,\tau|\varepsilon,\xi,\delta,0) v_j^{tr}(\varepsilon,\xi,delta,0) \mathrm{d}\delta \mathrm{d}\xi \mathrm{d}\varepsilon \right) \right\} \end{aligned} \tag{19}$$

To solve the above equation, it is essential to find the appropriate Green's function first, which is calculated from the homogeneous part of Eq. (12) by considering its homogeneous boundary conditions and initial condition given in Eq. (13) to Eq. (17). Then, the specified Green's function for transient heat distribution equation given in Eq. (12) can be obtained as [26–37]:

$$g_{ij}(x,y,z,\tau;\varepsilon,\xi,\delta,t) = \sum_{e=1}^{\infty} \sum_{f=1}^{\infty} \sum_{g=1}^{\infty} e^{-\lambda_{efg}(\tau-t)} \left( \frac{k_j}{\alpha_j} \right) \frac{X_{ie}^{tr}(x) X_{ie}^{tr}(\varepsilon) Y_f^{tr}(y) Y_f^{tr}(\xi) Z_g^{tr}(z) Z_g^{tr}(\delta)}{N_{xe} N_{yf} N_{zg}} \tag{20}$$

$$where;\ i,j = 1,2,3,\ldots,n$$

$$\lambda_{efg} = \lambda_{xe}^2 + \lambda_{yf}^2 + \lambda_{zg}^2 \tag{21}$$

where $g_{ij}$ is the Green's function associated with the $i$th tissue layer concerning the $j$th tissue layer; $\lambda_{xe}$, $\lambda_{yf}$, $\lambda_{zg}$ are the eigenvalues; $X_{ie}^{tr}(x)$, $Y_f^{tr}(y)$, $Z_g^{tr}(z)$ are the corresponding eigenfunctions; $N_{xe}$, $N_{yf}$, $N_{zg}$ are the respective norms and $e$, $f$, $g$ respective indices, in $x$, $y$, $z$ directions, respectively. $X_{ie}^{tr}(\varepsilon)$, $Y_f^{tr}(\xi)$, $Z_g^{tr}(\delta)$ are the eigenfunction in $\varepsilon$, $\xi$, $\delta$ directions respectively; the formulas to calculate the eigenfunction, eigenvalues, and norms have been given in the Appendix.

Now substituting Eq. (20) in Eq. (19) the solution for transient heat transfer is represented as [26–37]:

$$\begin{aligned} v_i^{tr} =& \left\{ \left( \int\limits_0^{\tau} \int\limits_{y_1}^{y_2} \int\limits_{z_1}^{z_2} \sum_{e=1}^{\infty} \sum_{f=1}^{\infty} \sum_{g=1}^{\infty} \left[ \frac{(-k_1) e^{-\left(\lambda_{xe}^2+\lambda_{yf}^2+\lambda_{zg}^2\right)(\tau-t)} X_{i,e}^{tr}(x) X_{j,e}^{tr}(\varepsilon) Y_f^{tr}(y) Y_f^{tr}(\xi) Z_g^{tr}(z) Z_g^{tr}(\delta)}{N_{xe} N_{yf} N_{zg}} \right. \right. \right. \\ & \left. \left. \left( \frac{\partial v_1^{tr}(\varepsilon,\xi,\delta,t)}{\partial x} \right) \right]_{\varepsilon=\varepsilon_1=0} \mathrm{d}\delta \mathrm{d}\xi \mathrm{d}t \right) \\ & + \sum_{j=1}^{n} \int\limits_{x_j}^{x_{j+1}} \int\limits_{y_1}^{y_2} \int\limits_{z_1}^{z_2} \left( \sum_{e=1}^{\infty} \sum_{f=1}^{\infty} \sum_{g=1}^{\infty} e^{-\left(\lambda_{xe}^2+\lambda_{yf}^2+\lambda_{zg}^2\right)\tau} \left( \frac{k_j}{\alpha_j} \right) \frac{X_{i,e}^{tr}(x) X_{j,e}^{tr}(\varepsilon) Y_f^{tr}(y) Y_f^{tr}(\xi) Z_g^{tr}(z) Z_g^{tr}(\delta)}{N_{xe} N_{yf} N_{zg}} \right. \\ & \left. \left. v_i^{tr}(\varepsilon,\xi,\delta,0) \mathrm{d}\delta \mathrm{d}\xi \mathrm{d}\varepsilon \right) \right\} \end{aligned} \tag{22}$$

Further substituting Eq. (13) in Eq. (22), the solution of transient heat transfer is converged to [26–37]:

$$\begin{aligned} v_i^{tr}(x,y,z,\tau) =& \left\{ \sum_{e=1}^{\infty} \left( \int\limits_0^{\tau} \left[ \frac{e^{-\lambda_{xe}^2(\tau-t)}}{N_{xe}} X_{i,e}^{tr}(x) X_{j,e}^{tr}(\varepsilon) q_H(t) \right] \mathrm{d}t \right) \right. \\ & \left. + \sum_{j=1}^{n} \left( \sum_{e=1}^{\infty} \int\limits_{x_j}^{x_{j+1}} \frac{e^{-\lambda_{xe}^2 \tau}}{N_{xe}} \left( \frac{k_j}{\alpha_j} \right) X_{i,e}^{tr}(x) X_{j,e}^{tr}(\varepsilon) v_i^{tr}(\varepsilon,\xi,\delta,0) \mathrm{d}\varepsilon \right) \right\} \end{aligned} \tag{23}$$

Eq. (23) provides the overall temporal thermal distribution over the modeled sample surface.

### 2.3. Solution for Digitized Frequency Modulated (DFM) Input

The incident excitation over the modeled sample surface (at $x = x_1 = 0$) is described as a time-dependent parameter. Here, the time-dependent DFM excitation (Figure 1(a)) used for DFMTWI of the breast model can be written as [23–25] follows:

$$q_1 = q_c \left( 1 + \frac{2}{\pi} \sum_{r=-\infty}^{\infty} \frac{(-1)^r}{2r+1} e^{-i2\pi(2r+1)\left(\mathrm{f}\tau + \frac{B\tau^2}{2T}\right)} \right), \quad at \quad x = 0 \tag{24}$$

where $q_1$ is the imposed heat flux (W/m$^2$); $q_c$ is the constant amplitude of heat flux (W/m$^2$); f, $B$, $\tau$, and T are the frequency (Hz), bandwidth (Hz), time variable (s), and total duration of applied heat flux. "$r$" represents the indices, and "$i$" is the complex number representation.

Then the overall solution for Pennes bioheat transfer equation Eq. (1) using Green's function approach for digitized frequency modulated thermal flux presented in Eq. (24) (Figure 1(a)) can be represented by Eq. (23) as:

$$\begin{aligned} v_i(x, y, z, \tau) &= v_i^{ss} + I_1 + I_2 + I_3 \\ &\quad + \sum_{e=1}^{\infty} \sum_{r=-\infty}^{\infty} \left[ \left( \frac{q_c \Psi X_{i,e}^{tr}(x)}{N_{xe} \pi^{\frac{3}{2}} (1+2r)^{\frac{3}{2}}} \right) e^{i\left(r\pi + \mathrm{f}^2\Psi^2(1+2r) - \frac{\eta^2}{(1+2r)} - \frac{\pi}{4}\right) - \frac{\Psi\omega\eta}{\pi}} \left( Erf[B_2] - Erf[B_1] \right) \right] \end{aligned} \tag{25}$$

$where; \quad i, j = 1, 2, 3, 4, 5, 6; \quad n = 6;$

The formulas to calculate the constant's value, eigenfunction, eigenvalues, and norms are given in the Appendix.

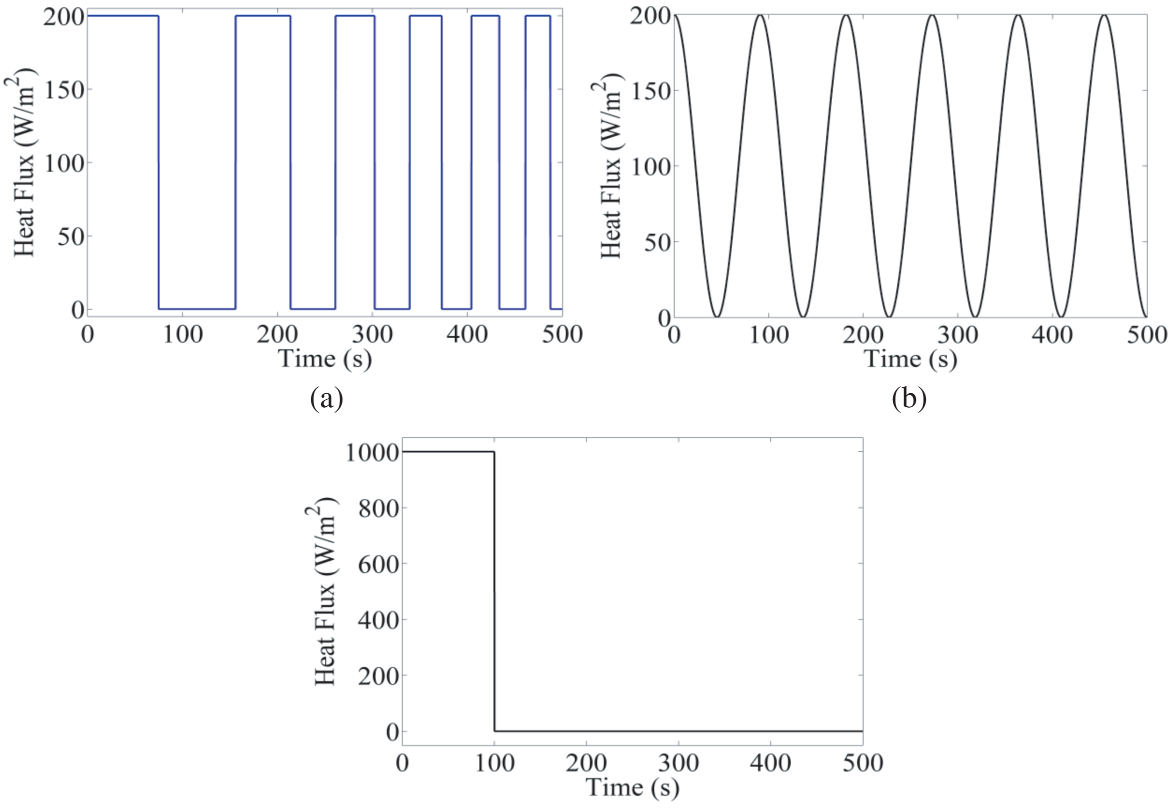

(a) (b)

(c)

**Figure 1.** Schematic of (a) digitized frequency modulated input heat flux having a frequency sweep of 0.002 Hz to 0.02 Hz, (b) periodically modulated input heat flux used for Lock-in thermography having a constant frequency of 0.011 Hz, (c) pulse input heat flux of on-time 100 seconds for a total duration of 500 seconds.

### 2.4. Solution for Periodically Modulated Input

After that, time-dependent periodically modulated input heat flux (Figure 1(b)) is used for the conventional Lock-in thermographic technique, which is mathematically written as [20–22]:

$$q_1 = q_c \left[1 + e^{-i\omega\tau}\right], \quad at \;\; x = 0 \qquad (26)$$
$$where: \quad \omega = 2\pi \mathrm{f}$$

For lock-in input presented by Eq. (26) and the graphical representation shown in Figure 1(b), its solution using Eq. (23) can be written as:

$$v_i\left(x, y, z, \tau\right) = v_i^{ss} + I_1 + I_2 + I_3 + \sum_{e=1}^{\infty} \left[\frac{q_c X_{i,e}^{tr}\left(x\right)}{N_{xe}} \left(\frac{e^{-i\omega\tau} - e^{-\lambda_{xe}^2 \tau}}{\lambda_{xe}^2 - i\omega}\right)\right] \qquad (27)$$
$$where: \quad i, j = 1, 2, 3, 4, 5, 6; \;\; n = 6$$

The formulas to calculate the constant's value, eigenfunction, eigenvalues, and norms are in the Appendix.

### 2.5. Solution for Pulse-Modulated Input

Further, the pulse input heat flux (Figure 1(c)) used for the conventional pulse thermographic technique is mathematically written as [16–19]:

$$q_1 = q_c \left[u(\tau) - u(\tau - \tau^*)\right], \quad x = 0 \qquad (28)$$

For pulse input presented by Eq. (28) and the graphical representation shown in Figure 1(c), its solution using Eq. (23) can be written mathematically as:

$$v_i\left(x, y, z, \tau\right) = v_i^{ss} + I_1 + I_2 + I_3 + \sum_{e=1}^{\infty} \left[\frac{q_c X_{e,i}^{tr}\left(x\right)}{N_{xe}} \left(\frac{1 - e^{-\lambda_{xe}^2 (\tau - \tau^*)}}{\lambda_{xe}^2}\right)\right] u(\tau - \tau^*) \qquad (29)$$

The formulas to calculate the constant's value, eigenfunction, eigenvalues, and norms are in the Appendix.

The present analytical models have been modeled for the quantitative estimation of breast cancer using DFMTWI and conventional thermographic techniques (LT and PT). Here, these models were mathematically presented by the multilayer Pennes bioheat transfer equation, mainly used for the theoretical studies of heat transfer in biological tissues. This equation provides information about the influence of blood perfusion on the temporal thermal distribution captured over the living tissue, which is written as in Eq. (1). This equation was solved using Green's function approach for adiabatic boundary conditions and constant initial condition for different thermographic techniques. Moreover, the interfacial boundary condition is considered a perfect thermal contact.

## 3. TIME-DOMAIN-BASED DATA PROCESSING APPROACH

Pulse compression-based signal processing techniques have been used predominantly to enhance the target detection ability in RADAR applications, which allows the transmission of long-duration modulated signals with low peak power over short-duration, high-peak-power signals. These techniques increase the radar system's overall resolution and detection capability. Further, pulse compression has been achieved by cross-correlation of the transmitted and reflected signals.

Hence, in this work, the time domain pulse compression-based data processing approach has been introduced for processing the data acquired analytically and numerically. The pulse compression has been achieved by cross-correlating the mean removed temporal thermal response obtained over the sound region (i.e., a healthy region where anomalies are not present) with the mean removed temporal thermal response received over the region where abnormalities are present, which is mathematically written as [38–41]:

$$CrossCorrelation \;\; (CC) = \int_{-\infty}^{+\infty} S_1(t) S_2(t - \tau) \mathrm{d}t \qquad (30)$$

where $S_1(t)$ is the mean removed temporal thermal response obtained over sound (healthy) regions; $S_2(t-\tau)$ is the mean removed temporal thermal response depicted over anomaly regions.

## 4. ABSOLUTE ERROR ESTIMATION

The analytical approaches presented in this research have been compared with the finite-element-based numerical simulation studies using the time domain-based pulse compression approaches by taking the correlation coefficient as a figure of merit. An absolute error has been calculated to determine the variation between the solutions obtained using analytical and numerical studies.

The mathematical formulation for absolute error is given as follows:

$$Absolute\ error = |Exact\ Value - Approximated\ Value| \tag{31}$$

Analytical approaches yield exact values within this context, whereas numerical methods provide approximated values.

## 5. NUMERICAL MODELING AND SIMULATION

Three-dimensional multilayer breast models (Figure 2) consisting of tumors were modeled using commercially available finite element modeling (FEM) and assessment software COMSOL Multiphysics. The models comprise four different layers: skin, fat, gland, and muscle of thicknesses 1.7 mm, 2 mm, 44 mm, and 22 mm, respectively, having other thermophysical properties as described in Table 1. The overall dimensions of the models are presented in Figure 2. These models were solved by considering the multilayer Pennes bioheat transfer equation for adiabatic boundary conditions and constant initial temperature conditions of 310.15 K, which is the basal state temperature of the human body. Numerical studies were performed on two separate breast models. The first breast model (Figure 2(a)) was studied with and without a tumor, considering one tumor at a time. However, the second breast model was analyzed by considering four tumors at different locations (Table 2) of similar shapes and sizes mentioned in Figure 2(b).

The skin surface of the breast model is exposed to pulse input (Figure 1(c)) of on-time 100 seconds for PT, a periodically modulated heat flux of constant frequency of 0.011 Hz (Figure 1(b)) for LT, and a

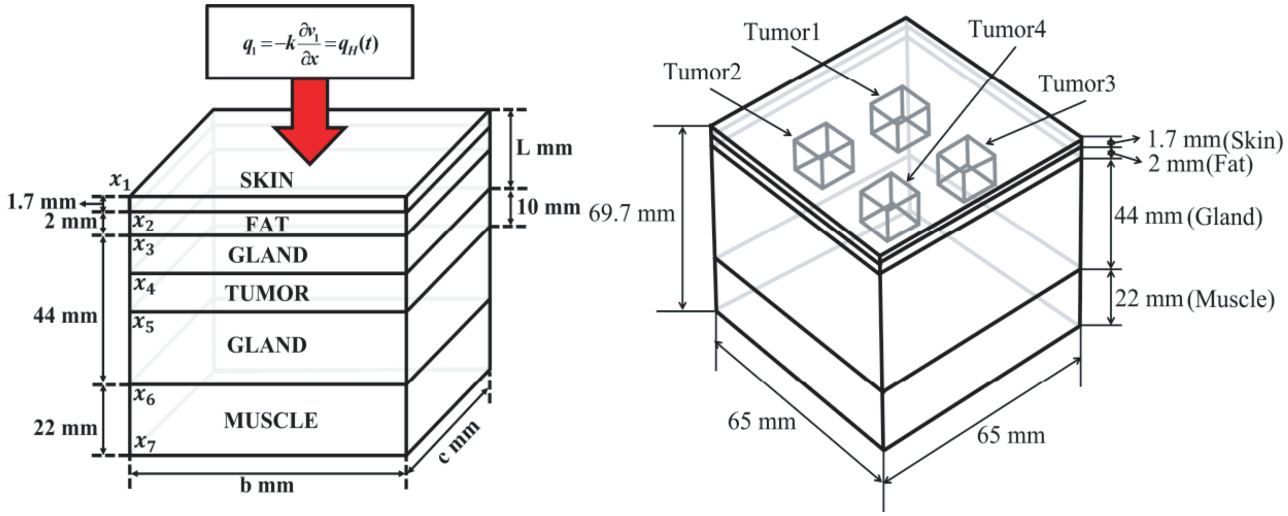

(a) (b)

**Figure 2.** Schematic of multilayer breast models used for simulation studies. (a) The first simulation model, S1, consisted of a cross-section of the breast with a single embedded tumor. (b) The second simulation model, S2, included four tumors of similar shape and size positioned at different depths beneath the surface of the modeled sample.

**Table 1.** Thermo-physical properties of different layers of modeled breast model [42–45].

| **Region** | **Density** ($\rho$) (kg/m$^3$) | **Thermal Conductivity** ($K$) (W/mK) | **Specific Heat** ($c_p$) (J/kg · K) | **Blood Perfusion** ($w_b$) ((ml/s)/ml) | **Metabolic Heat Generation Rate** ($Q_m$) (W/m$^3$) |
|---|---|---|---|---|---|
| Skin | 1085 | 0.47 | 3680 | 0.002 | 368.1 |
| Fat | 930 | 0.21 | 2770 | 0.0002 | 400 |
| Gland | 1050 | 0.48 | 3770 | 0.0006 | 700 |
| Muscle | 1100 | 0.48 | 3800 | 0.0009 | 700 |
| Tumour | 1050 | 0.48 | 3852 | 0.012 | 29000 |

**Table 2.** Tumor depth from the surface of modeled breast sample.

| **Sr. No.** | **Tumor** | **Depth ($L$) (mm)** |
|---|---|---|
| T1 | Tumor1 | 4 |
| T2 | Tumor2 | 5 |
| T3 | Tumor3 | 6 |
| T4 | Tumor4 | 7 |
| *The breast model without tumors has been presented by HB notation in further discussion | | |

digitized frequency modulated input heat flux (Figure 1(a)) with frequency sweep of 0.002 Hz to 0.2 Hz for DFMTWI respectively for a total duration of 500 seconds. Consequently, the temporal thermal variations were recorded. Furthermore, to validate the analytical technique provided in the preceding section, the numerically generated thermal data is compared to the analytically acquired thermal data using Eq. (23), with the correlation coefficient as a figure of merit for the quantitative estimation of breast cancer.

## 6. RESULT AND DISCUSSION

An analytical solution for three-dimensional multilayer Pennes bioheat transfers equation Eq. (1) for an imposed digitized frequency modulated heat flux (Figure 1(a)) with a frequency sweep of 0.002–0.02 Hz for 500 seconds (Eq. (24)) has been presented in the current study for the quantitative estimation of breast cancer at earlier stages. The temporal thermal response over the breast model (Figure 2(a)) surface has been obtained analytically using Eq. (25) for the tumor located at different depths from the modeled sample surface presented in Figure 3(a). The breast model without a tumor (HB) exhibits a lower thermal signature than the breast model containing a tumor at various depths. The captured thermal response increases from Tumor-4 (T4) to Tumor-1 (T1), because the breast with a tumor has a higher blood perfusion rate and a higher metabolic internal heat generation rate. It is due to the cancer cells, which increase blood perfusion and metabolic internal heat generation rate. It leads to increases in the overall temporal thermal signature over the skin surface of modeled breast sample at the location where the tumor presents. To apply the time domain-based correlation approach over the obtained temporal thermal data (Figure 3(a)), the mean rise due to the active heating must be removed by suitable fitting to recreate mean zero thermal profiles. It has been achieved by polynomial fitting of the acquired data. After that, the obtained mean extracted thermal responses from the breast without tumor (HB) and responses received from the tumor at different locations (shown in Table 2) were correlated. Then the normalized correlation coefficient variations with time have been obtained,

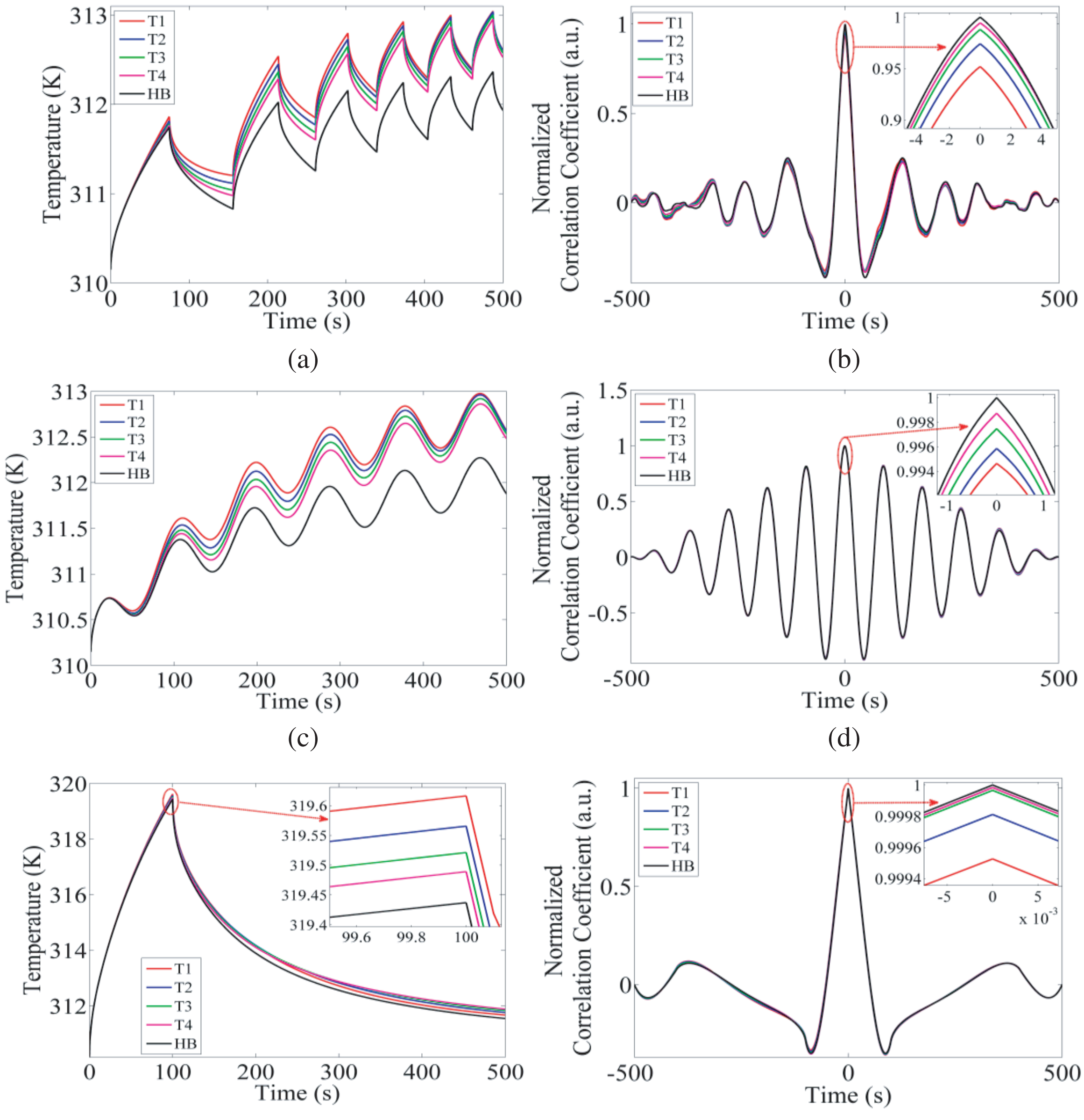

(a) (b) (c) (d) (e) (f)

**Figure 3.** Schematic representation of 3D multilayer analytical solution results for quantitative estimation of breast cancer. (a) Temporal thermal distribution obtained over sample surface for digitised modulated imposed thermal heat flux as presented in Figure 1(a). (b) Corresponding normalized correlation coefficient response. (c) Temporal thermal distribution obtained over sample surface for periodically modulated imposed thermal heat flux as presented in Figure 1(b). (d) Corresponding normalized correlation coefficient response. (e) Temporal thermal distribution obtained over sample surface for pulse incident thermal heat flux as shown in Figure 1(c). (f) Corresponding normalized correlation coefficient response.

which is shown in Figure 3(b).

Further, these analytical results were compared with the simulated ones for validation in the quantitative estimation of breast cancer. The simulation model presented in this study involves the solution of two sets of models. In the first set of breast model (S1), one tumor at a time has been modeled, and temporal thermal variations are recorded for DFMTWI, as shown in Figure 4(a). Similar

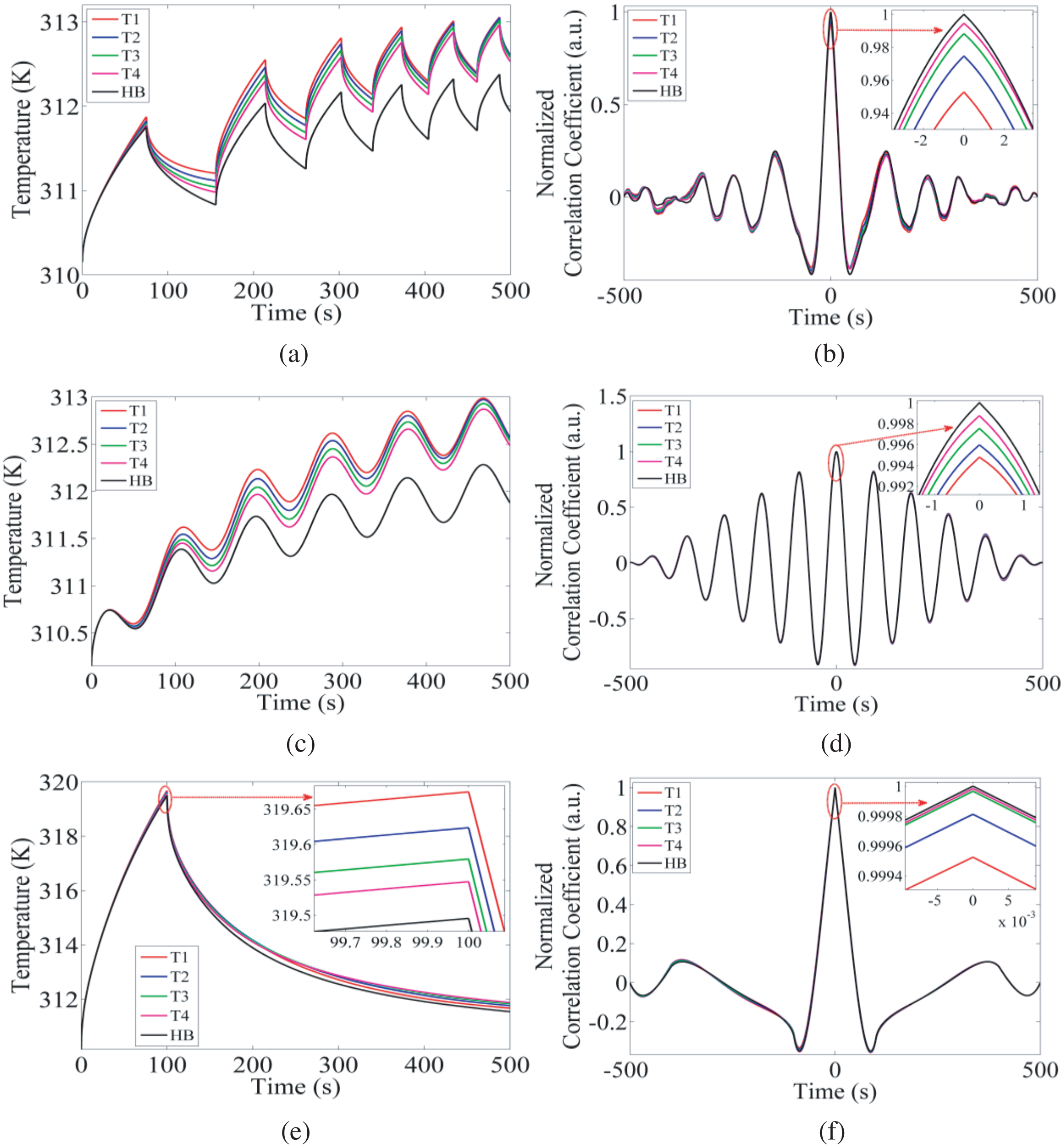

**Figure 4.** Schematic representation of first 3D multilayer simulation model S1 results for quantitative estimation of breast cancer. (a) Temporal thermal distribution obtained over sample surface for digitised modulated imposed thermal heat flux presented in Figure 1(a). (b) Corresponding normalized correlation coefficient response. (c) Temporal thermal distribution obtained over sample surface for periodically modulated imposed thermal heat flux as presented in Figure 1(b). (d) Corresponding normalized correlation coefficient response. (e) Temporal thermal distribution obtained over sample surface for pulse incident thermal heat flux as shown in Figure 1(c). (f) Corresponding normalized correlation coefficient response.

data processing approaches have been applied over the obtained data as applied over the analytical data, and the results obtained are presented in Figure 4(b). The main difference among the solutions obtained analytically and numerically arises in the magnitude values and not in the trend followed by their responses. The numerically obtained results have higher values than the analytically obtained

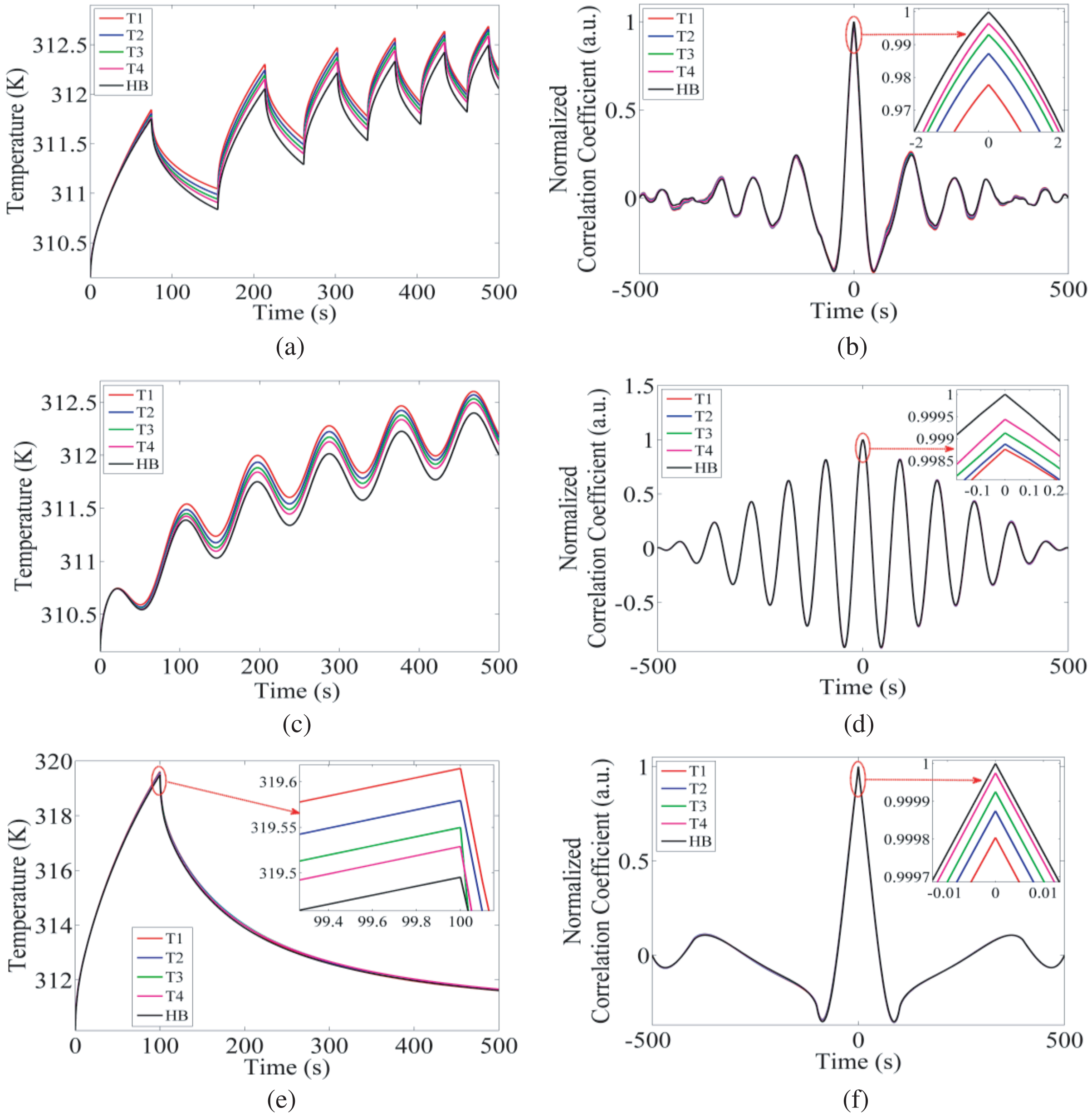

**Figure 5.** Schematic representation of second 3D multilayer simulation model S2 results for quantitative estimation of breast cancer. (a) Temporal thermal distribution obtained over sample surface for digitised modulated imposed thermal heat flux presented in Figure 1(a). (b) Corresponding normalized correlation coefficient response. (c) Temporal thermal distribution obtained over sample surface for periodically modulated imposed thermal heat flux presented in Figure 1(b). (d) Corresponding normalized correlation coefficient response. (e) Temporal thermal distribution obtained over sample surface for pulse incident thermal heat flux as shown in Figure 1(c). (f) Corresponding normalized correlation coefficient response.

results.

Simultaneously in the second model (S2), all the tumors are embedded at the same time in the modeled sample at 4 mm, 5 mm, 6 mm, and 7 mm depths, respectively, and the corresponding thermal variations are recorded (as shown in Figure 5(a)). However, the thermal profiles obtained in this case has low magnitude compared to that of analytically obtained thermal profiles without changing the trend (T1 > T2 > T3 > T4) they follow. It is due to the influence of the thermal distribution of all the tumors modeled simultaneously in the model. Thereafter, similar data processing approaches have been applied to the obtained simulation data as applied to analytical data, and the results obtained are presented in Figure 5(b).

A further similar procedure has been followed for LT where a sinusoidally modulated heat flux (as shown in Figure 1(b)) of modulating frequency 0.011 Hz with a peak power of $200\,\mathrm{W/m^2}$ for a time duration of 500 seconds is imposed over the modeled test object (Figure 2). Then the temporal thermal variation over the modeled sample has been calculated analytically by Eq. (27), as presented in Figure 3(c). To utilize pulse compression-based effective data processing techniques on the acquired thermal data, and it is necessary to remove the average mean rise from the dynamic data. It has been achieved by polynomial fitting of the obtained data. This means extracted data processed with a time domain-based cross-correlation approach, and the results are shown in Figure 3(d). The analytical results are subsequently cross-checked against the numerical results obtained through Lock-in Thermography. Specifically, Figure 4(c), Figure 4(d), Figure 5(c), and Figure 5(d) depict the temporal thermal distribution for simulation model S1, the correlation coefficient response for the S1 model, the temporal thermal distribution for simulation models S2, and the correlation coefficient response for S2 model, respectively. The results obtained analytically and numerically in the case of LT show a similar relationship to that observed for the analytical and simulated results of DFMTWI.

Lastly, a similar procedure has been followed up for the analytical approach (Eq. (29)) for Pulse Thermography (PT), with an input heat flux of on-time 100 seconds and a total duration of 500 seconds (Figure 1(c)) with a peak power of $1000\,\mathrm{W/m^2}$ imposed over the modeled sample surface (Figure 2). Figure 3(e) and Figure 3(f) depict the analytically obtained temporal thermal profiles and the correlation coefficient response, respectively. Furthermore, Figure 4(e), Figure 4(f), Figure 5(e), and Figure 5(f) depict the thermal response and corresponding correlation coefficient response for S1 and S2 numerical models, respectively. The analytically and numerically obtained results for pulse thermography application also follow the same trends as depicted in LT and DFMTWI.

To analyze the detection capability for the proposed DFMTWI technique concerning conventional thermography techniques such as PT and LT, the analytically obtained cross-correlation responses depicted for T1, T2, T3, and T4 are presented in Figure 6(a) to Figure 6(d), respectively. From Figure 6, it can be visualized that the proposed DFMTWI technique shows high pulse compression properties. Hence, concentrate the maximum supplied energy into the main lobe, and a minimal amount of energy is distributed to the side lobes compared to conventional thermographic techniques such as PT and LT. It helps distinguish the signal from the noise and improves the sensitivity and resolution for diagnosing tumors at early stages compared to conventional thermographic techniques such as PT and LT. Contrastingly, in the case of PT, an equal amount of energy is dispersed in the main lobe and side lobes. As a result, the pulse cannot be compressed to a narrow duration, limiting its pulse compression properties.

Similarly, LT fails to provide pulse compression due to lack of its energy concentration capabilities to a localized narrow time duration. It arises due to the utilization of a mono-frequency mode which limits the depth resolution. The analytically and numerically obtained correlation coefficient values for conventional (PT and LT) and proposed DFMTWI thermographic techniques have been plotted with the tumor depths, as presented in Figure 7. It has been analyzed that the proposed DFMTWI technique shows a higher slope with a monotonically increasing trend as the tumor depth rises from the modeled sample surface. It is because the DFMTWI technique probes fundamental components of frequencies ranging from 0.002 to 0.2 Hertz, as well as their corresponding harmonics, within breast samples which enhances test resolution and sensitivity. The constant trend of correlation coefficient values with tumor depths in PT studies has been illustrated in Figure 7. It is due to the high amplitude of heat flux (Figure 1(c)) used in the study, which would cause damage to the sample surface if being applied for an extended period. As a result, the temperature signature over the skin surface of the modeled sample would increase and prevent the formation of a gradient. Consequently, the thermal responses depicted in Figure 3(e), Figure 4(e), and Figure 5(e) for different depths of the tumor do not vary much. When LT is used, the penetration depth of the thermal wave inside the test sample is restricted due to the mono frequency used, resulting in a limited analysis of significant variations as indicated in Figure 7. Through all these studies, it has been analyzed that detecting early-stage breast cancer is closely linked

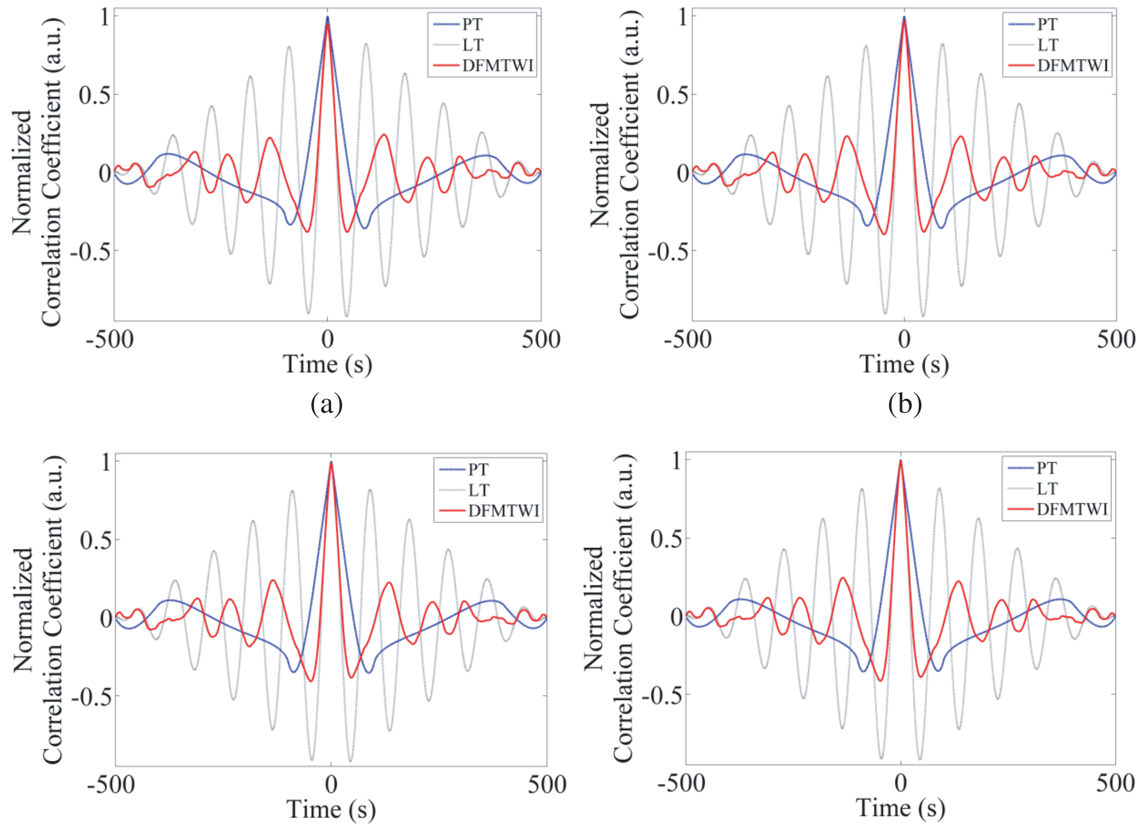

(a) (b)

(c) (d)

**Figure 6.** Comparison of correlation response of PT, LT, and DFMTWI techniques for different tumor depths, i.e., (a) 4 mm, (b) 5 mm, (c) 6 mm, and (d) 7 mm, respectively.

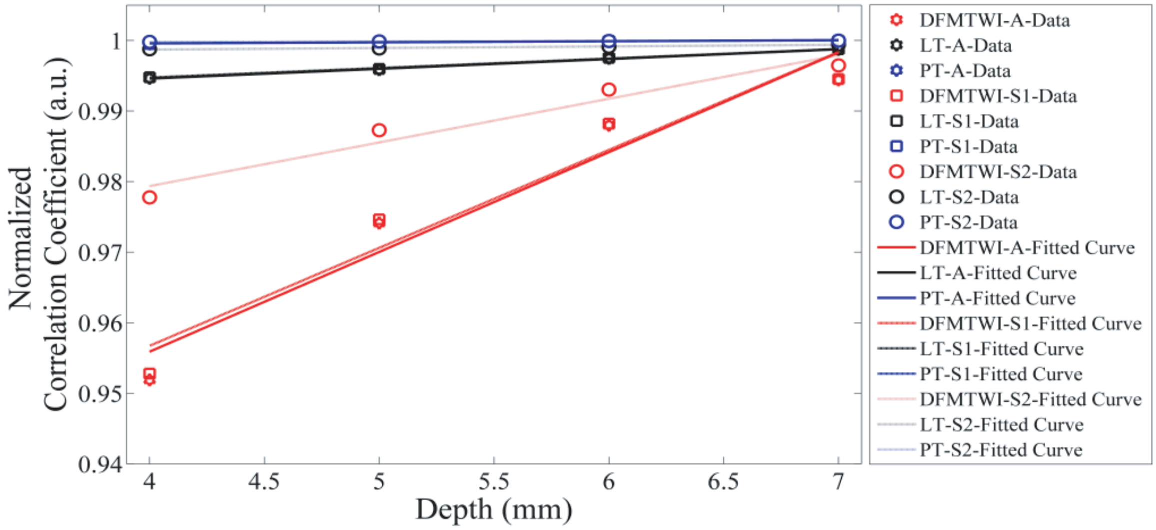

**Figure 7.** Comparison of correlation response with different tumor depths from breast sample surface (Table 3.4) for PT, LT, and DFMTWI techniques, respectively.

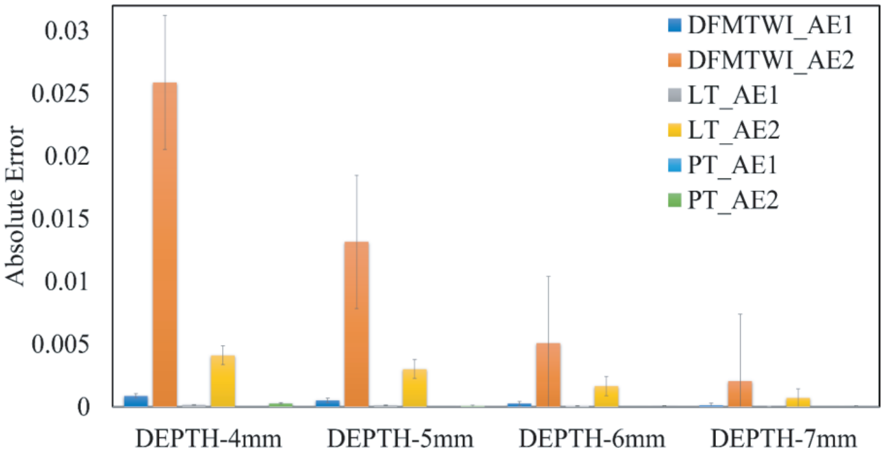

**Figure 8.** Schematic representation of absolute error between the analytically and the numerically obtained normalized correlation coefficient responses for different tumor depths.

to the correlation coefficient's significance concerning the variation of tumor depth from the modeled sample surface. Furthermore, Figure 8 shows the absolute error between the correlation coefficient values obtained analytically and numerically for the proposed DFMTWI technique and conventional thermographic techniques.

## 7. CONCLUSION

An analytical model has been utilized to present the quantitative estimation of breast cancer detection capabilities of the proposed Digitized Frequency Modulated Thermal Wave Imaging (DFMTWI) technique. The evaluation was conducted using pulsed compression-based time domain cross-correlation methodologies as a figure of merit. Analytically obtained results have been validated with the finite element-based software results. This similar set of analytical, numerical, and data evaluation techniques has been implemented over the conventional thermographic techniques PT and LT. The analytically and numerically obtained results for simulation model S1 depict the high similarity in the thermal and the correlation coefficient responses compared to the simulation model S2. In simulation model S2, the absolute error obtained is higher than that of model S1 because all the tumors are modeled simultaneously in the breast model. It decreases the overall thermal distribution over the modeled breast sample. Further, it can be concluded from the above study that the DFMTWI technique with pulse compression-based data processing approach, such as time domain-based cross-correlation, signifies improved sensitivity, and resolution for early detection and quantitative estimation of breast cancer. It allows the DFMTWI pulse to be compressed to a limited duration and localizes the maximum energy provided in the main lobe compared to conventional thermographic techniques such as PT and LT.

## APPENDIX A.

This Appendix briefly presents calculations related to eigenvalues, eigenfunctions, norms, integrals, variables, and constants required in the initial analysis. Some estimates are reproduced from references [29–40], while others have been derived here in this study.

### A1. Eigenfunction Calculation

$x$-direction:

$$X_{i,e}^{tr}(x) = A_{ie}\mathrm{Cos}\left(\sqrt{\left(\frac{\lambda_{xe}^2-\phi_i}{\alpha_i}\right)}x\right) + B_{ie}\mathrm{Sin}\left(\sqrt{\left(\frac{\lambda_{xe}^2-\phi_i}{\alpha_i}\right)}x\right) \tag{A1}$$

$$X_{j,e}^{tr}(\varepsilon) = A_{je}\mathrm{Cos}\left(\sqrt{\left(\frac{\lambda_{xe}^2-\phi_j}{\alpha_j}\right)}\varepsilon\right) + B_{je}\mathrm{Sin}\left(\sqrt{\left(\frac{\lambda_{xe}^2-\phi_j}{\alpha_j}\right)}\varepsilon\right) \tag{A2}$$

$y$-direction:

$$\left.\begin{array}{l} Y_f^{tr}(y) = \mathrm{Cos}(\lambda_{yf}y) \\ Y_f^{tr}(\xi) = \mathrm{Cos}(\lambda_{yf}\xi) \end{array}\right\} \tag{A3}$$

$z$-direction:

$$\left.\begin{array}{l} Z_g^{tr}(z) = \mathrm{Cos}(\lambda_{zg}z) \\ Z_g^{tr}(\delta) = \mathrm{Cos}(\lambda_{zg}\delta) \end{array}\right\} \tag{A4}$$

However, in the eigenfunction, $X_{i,e}^{tr}(x)$, the constant-coefficient $A_{ie}$ and $B_{ie}$ values are calculated using $2n$ number of linear homogeneous equations obtained from boundary conditions. The determinant of the matrix obtained by these $2n$ number of equations equal to zero leads to a trivial solution for these systems of equations. Setting upon the determinant of the matrix obtained to zero gives a transcendental equation, which is further solved to determine the infinite number of eigenvalues $\lambda_{xe}$, where $e = 1, 2, 3 \ldots \infty$ [26–37].

## A2. Norms Calculations

$x$-direction:

$$N_{xe} = \sum_{j=1}^{n}\left(\frac{k_j}{\alpha_j}\right)\int_{x_j}^{x_{j+1}}\left(X_{j,e}^{tr}(\varepsilon)\right)^2 d\varepsilon; \quad where: \quad e = 1, 2, 3, \ldots. \tag{A5}$$

$y$-direction:

$$N_{yf} = \int_{y_1=0}^{y_2=b}\left(Y_f^{tr}(\xi)\right)^2 d\xi = \int_{y_1=0}^{y_2=b}\left(\mathrm{Cos}(\lambda_{yf}\xi)\right)^2 d\xi = \left\{\frac{b}{2}; \quad where: \ f = 1, 2, 3, \ldots. \right. \tag{A6}$$

$z$-direction:

$$N_{zg} = \int_{z_1=?0}^{z_2=c}\left(Z_g^{tr}(\delta)\right)^2 d\delta = \int_{z_1=0}^{z_2=c}\left(\mathrm{Cos}(\lambda_{zg}\delta)\right)^2 d\delta = \left\{\frac{c}{2} \quad where: \ g = 1, 2, 3, \ldots. \right. \tag{A7}$$

## A3. Constants, Variables, and Integrals Calculations

$$\omega = 2\pi\left(\mathrm{f} + \frac{B\tau}{\mathcal{T}}\right) \tag{A8}$$

$$\Psi = \sqrt{\frac{\pi\mathcal{T}}{B}} \quad and \quad \eta = \frac{\Psi\lambda_{xe}^2}{2\pi} \tag{A9}$$

$$B_1 = \frac{e^{\frac{\pi}{4}i}}{\sqrt{1+2r}}\left[\mathrm{f}\Psi(1+2r) + i\eta\right] \tag{A10}$$

$$B_2 = \frac{e^{\frac{\pi}{4}i}}{\sqrt{1+2r}}\left[\frac{\omega\Psi}{2\pi}(1+2r) + i\eta\right] \tag{A11}$$

$$\varphi_j = \left(\frac{w_{bj}\rho_b c_b}{k_j}\right) \quad and \quad \varphi_i = \left(\frac{w_{bi}\rho_b c_b}{k_i}\right) \tag{A12}$$

$$\phi_j = \left(\frac{w_{bj}\rho_b c_b}{\rho_j c_{\mathrm{p}j}}\right) \quad and \quad \phi_i = \left(\frac{w_{bi}\rho_b c_b}{\rho_i c_{\mathrm{p}i}}\right) \tag{A13}$$

$$I_1 = \sum_{e=1}^{\infty} \frac{q_c X_{i,e}^{tr}(x)}{N_{xe}} \left( \frac{1 - e^{-\lambda_{xe}^2 \tau}}{\lambda_{xe}^2} \right) \tag{A14}$$

$$I_2 = \sum_{j=1}^{n} \sum_{e=1}^{\infty} \left[ \frac{k_j X_{i,e}^{tr}(x)\, e^{-\lambda_{xe}^2 \tau}}{N_{xe} \sqrt{\alpha_j} \sqrt{\lambda_{xe}^2 - \phi_j}} \left( v_{0j} - v_a - \frac{q_{mj}}{w_{bj} \rho_b c_b} \right) N_{j,e} \right] \tag{A15}$$

$$I_3 = -\sum_{j=1}^{n} \sum_{e=1}^{\infty} \frac{k_j e^{-\lambda_{xe}^2 \tau} X_{i,e}^{tr}}{N_{xe} \lambda_{xe}^2} \left\{ \begin{array}{l} \left[ \mathrm{P}_{j,e} \left( B_{je} D_j \sqrt{\varphi_j} + A_{je} E_j \sqrt{\dfrac{\lambda_{xe}^2 - \phi_j}{\alpha_j}} \right) \right] \\ + \left[ \mathrm{Q}_{j,e} \left( A_{je} E_j \sqrt{\varphi_j} - B_{je} D_j \sqrt{\dfrac{\lambda_{xe}^2 - \phi_j}{\alpha_j}} \right) \right] \\ + \left[ \mathrm{R}_{j,e} \left( B_{je} E_j \sqrt{\varphi_j} + A_{je} D_j \sqrt{\dfrac{\lambda_{xe}^2 - \phi_j}{\alpha_j}} \right) \right] \\ + \left[ \mathrm{S}_{j,e} \left( A_{je} D_j \sqrt{\varphi_j} - B_{je} E_j \sqrt{\dfrac{\lambda_{xe}^2 - \phi_j}{\alpha_j}} \right) \right] \end{array} \right\} \tag{A16}$$

$$N_{j,e} = \left[ \begin{array}{l} A_{je} \left[ \mathrm{Sin} \left( \sqrt{\dfrac{\lambda_{xe}^2 - \phi_j}{\alpha_j}} x_{j+1} \right) - \mathrm{Sin} \left( \sqrt{\dfrac{\lambda_{xe}^2 - \phi_j}{\alpha_j}} x_j \right) \right] \\ -B_{je} \left[ \mathrm{Cos} \left( \sqrt{\dfrac{\lambda_{xe}^2 - \phi_j}{\alpha_j}} x_{j+1} \right) - \mathrm{Cos} \left( \sqrt{\dfrac{\lambda_{xe}^2 - \phi_j}{\alpha_j}} \right) x_j \right] \end{array} \right] \tag{A17}$$

$$\mathrm{P}_{j,e} = \left( \mathrm{Sin} \left( \sqrt{\frac{\lambda_{xe}^2 - \phi_j}{\alpha_j}} x_{j+1} \right) \mathrm{Sinh} \left( \sqrt{\varphi_j} x_{j+1} \right) - \mathrm{Sin} \left( \sqrt{\frac{\lambda_{xe}^2 - \phi_j}{\alpha_j}} x_j \right) \mathrm{Sinh} \left( \sqrt{\varphi_j} x_j \right) \right) \tag{A18}$$

$$\mathrm{Q}_{j,e} = \left( \mathrm{Cos} \left( \sqrt{\frac{\lambda_{xe}^2 - \phi_j}{\alpha_j}} x_{j+1} \right) \mathrm{Cosh} \left( \sqrt{\varphi_j} x_{j+1} \right) - \mathrm{Cos} \left( \sqrt{\frac{\lambda_{xe}^2 - \phi_j}{\alpha_j}} x_j \right) \mathrm{Cosh} \left( \sqrt{\varphi_j} x_j \right) \right) \tag{A19}$$

$$\mathrm{R}_{j,e} = \left( \mathrm{Cosh} \left( \sqrt{\varphi_j} x_{j+1} \right) \mathrm{Sin} \left( \sqrt{\frac{\lambda_{xe}^2 - \phi_j}{\alpha_j}} x_{j+1} \right) - \mathrm{Cosh} \left( \sqrt{\varphi_j} x_j \right) \mathrm{Sin} \left( \sqrt{\frac{\lambda_{xe}^2 - \phi_j}{\alpha_j}} x_j \right) \right) \tag{A20}$$

$$\mathrm{S}_{j,e} = \left( \mathrm{Cos} \left( \sqrt{\frac{\lambda_{xe}^2 - \phi_j}{\alpha_j}} x_{j+1} \right) \mathrm{Sinh} \left( \sqrt{\varphi_j} x_{j+1} \right) - \mathrm{Cos} \left( \sqrt{\frac{\lambda_{xe}^2 - \phi_j}{\alpha_j}} x_j \right) \mathrm{Sinh} \left( \sqrt{\varphi_j} x_j \right) \right) \tag{A21}$$

## REFERENCES

1. Bray, F., J. Ferlay, I. Soerjomataram, et al., "Global cancer statistics 2018: GLOBOCAN estimates of incidence and mortality worldwide for 36 cancers in 185 countries," *CA Cancer J. Clin.*, Vol. 68, 394–424, 2018.
2. Ferlay, J., M. Colombet, I. Soerjomataram, C. Mathers, D. M. Parkin, M. Piñeros, A. Znaor, and F. Bray, "Estimating the global cancer incidence and mortality in 2018: GLOBOCAN sources and methods," *International Journal of Cancer*, Vol. 144, No. 8, 1941–1953, 2019.
3. Riggio, A. I., K. E. Varley, and A. L. Welm, "The lingering mysteries of metastatic recurrence in breast cancer," *British Journal of Cancer*, Vol. 124, No. 1, 13–26, 2021.
4. Hassett, M. J., M. R. Somerfield, E. R. Baker, F. Cardoso, K. J. Kansal, D. C. Kwait, and S. H. Giordano, "Management of male breast cancer: ASCO guideline," *Journal of Clinical Oncology*, Vol. 38, No. 16, 1849–1863, 2020.

5. Hortobagyi, G. N., J. de la Garza Salazar, K. Pritchard, D. Amadori, R. Haidinger, and C. A. Hudis, "ABREAST investigators, the global breast cancer burden: Variations in epidemiology and survival," *Clinical Breast Cancer*, Vol. 6, No. 5, 391–401, 2005.
6. He, Z., Z. Chen, M. Tan, S. Elingarami, Y. Liu, T. Li, and W. Li, "A review on methods for diagnosis of breast cancer cells and tissues," *Cell Proliferation*, Vol. 53, No. 7, e12822, 2020.
7. Harbeck, N., F. Penault-Llorca, J. Cortes, M. Gnant, N. Houssami, P. Poortmans, K. Ruddy, J. Tsang, and F. Cardoso, "Breast cancer (Primer)," *Nature Reviews: Disease Primers*, Vol. 5, No. 1, 66, 2019.
8. Britt, K. L., J. Cuzick, and K. A. Phillips, "Key steps for effective breast cancer prevention," *Nature Reviews Cancer*, 1–20, 2020.
9. Akram, M., M. Iqbal, M. Daniyal, and A. U. Khan, "Awareness, and current knowledge of breast cancer," *Biological Research*, Vol. 50, No. 1, 33, 2017.
10. Rao, A. P., N. Bokde, and S. Sinha, "Photoacoustic imaging for management of breast cancer: A literature review and future perspectives," *Applied Sciences*, Vol. 10, No. 3, 767, 2020.
11. Zeng, Z., A. Amin, A. Roy, N. E. Pulliam, L. C. Karavites, S. Espino, I. Helenowski, X. Li, Y. Luo, and S. A. Khan, "Preoperative magnetic resonance imaging use and oncologic outcomes in premenopausal breast cancer patients," *NPJ Breast Cancer*, Vol. 6, No. 1, 1–8, 2020.
12. Badiger, S. and J. Moger, "A comparative study of mammography, sonography and infrared thermography in detection of cancer in breast," *International Surgery Journal*, Vol. 7, No. 6, 1886–1892, 2020.
13. Wang, J., K. J. Chang, C. Y. Chen, K. L. Chien, Y. S. Tsai, Y. M. Wu, and T. T. F. Shih, "Evaluation of the diagnostic performance of infrared imaging of the breast: A preliminary study," *Biomedical Engineering Online*, Vol. 9, No. 1, 1–14, 2010.
14. Ng, E. Y. K. and N. M. Sudharsan, "An improved three-dimensional direct numerical modelling and thermal analysis of a female breast with tumour," *Proceedings of the Institution of Mechanical Engineers, Part H: Journal of Engineering in Medicine*, Vol. 215, No. 1, 25–37, 2001.
15. González, F. J., "Noninvasive estimation of the metabolic heat production of breast tumors using digital infrared imaging," *Quantitative InfraRed Thermography Journal*, Vol. 8, No. 2, 139–148, 2011.
16. Maldague, X. and S. Marinetti, "Pulse phase infrared thermography," *Journal of Applied Physics*, Vol. 79, No. 5, 2694–2698, 1996.
17. Maldague, X., Y. Largouct, and J. P. Couturier, "A study of defect depth using neural networks in pulsed phase thermography: Modeling, noise, experiments," *Revue Generale de Thermique*, Vol. 37, No. 8, 704–717, 1998.
18. Vavilov, V. P. and S. Marinetti, "Pulsed phase thermography and fourier-analysis thermal tomography, *Russian Journal of Nondestructive Testing*, Vol. 35, No. 2, 134–145, 1999.
19. Ibarra-Castanedo, C., N. P. Avdelidis, and X. Maldague, "Qualitative and quantitative assessment of steel plates using pulsed phase thermography," *Materials Evaluation*, Vol. 63, No. 11, 1128–1133, 2005.
20. Pickering, S. and D. Almond, "Matched excitation energy comparison of the pulse and lock-in thermography NDE techniques," *NDT and E International*, Vol. 41, No. 7, 501–509, 2008.
21. Busse, G., D. Wu, and W. Karpen, "Thermal wave imaging with phase sensitive modulated thermography," *Journal of Applied Physics*, Vol. 71, No. 8, 3962–3965, 1992.
22. Wu, D. and G. Busse, "Lock-in thermography for Nondestructive evaluation of materials," *Revue Generale de Thermique*, Vol. 37, No. 8, 693–703, 1998.
23. Mulaveesala, R. and S. Tuli, "Digitized frequency modulated thermal wave imaging for nondestructive testing," *Materials Evaluation*, Vol. 63, No. 10, 1046–1050, 2005.
24. Mulaveesala, R., P. Pal, and S. Tuli, "Interface study of bonded wafers by digitized linear frequency modulated thermal wave imaging," *Sensors and Actuators A: Physical*, Vol. 128, No. 1, 209–216, 2006.

25. Sharma, A., R. Mulaveesala, G. Dua, V. Arora, and N. Kumar, "Digitized frequency modulated thermal wave imaging for detection and estimation of osteoporosis," *IEEE Sensors Journal*, Vol. 21, No. 13, 14003–14010, 2021.
26. Carslaw, H. S. and J. C. Jaeger, *Conduction of Heat in Solids*, Oxford Clarendon Press, London, 1959.
27. Özısık, M. N., *Heat Conduction*, John Wiley & Sons, 1993.
28. Özısık, M. N., *Boundary Value Problems of Heat Conduction*, Courier Corporation, 1989.
29. Pennes, H. H., "Analysis of tissue and arterial blood temperatures in the resting human forearm," *Journal of Applied Physiology*, Vol. 1, No. 2, 93–122, 1948.
30. Durkee, Jr., J., P. Antich, and C. Lee, "Exact solutions to the multiregion time-dependent bioheat equation. I: Solution development," *Physics in Medicine* & *Biology*, Vol. 35, No. 7, 847, 1990.
31. Durkee, Jr., J., P. Antich, and C. Lee, "Exact solutions to the multiregion time-dependent bioheat equation. II: Numerical evaluation of the solutions," *Physics in Medicine* & *Biology*, Vol. 35, No. 7, 869, 1990.
32. Durkee, Jr., J. and P. Antich, "Exact solutions to the multi-region time-dependent bioheat equation with transient heat sources and boundary conditions," *Physics in Medicine* & *Biology*, Vol. 36, No. 3, 345, 1991.
33. Sharma, A., R. Mulaveesala, and V. Arora, "Novel analytical approach for estimating thermal diffusivity and effusivity for detection of osteoporosis," *IEEE Sensors Journal*, Vol. 20, No. 11, 6046–6054, 2020.
34. Sharma, A., R. Mulaveesala, G. Dua, and N. Kumar, "Linear frequency modulated thermal wave imaging for estimation of osteoporosis: An analytical approach," *Electronics Letters*, Vol. 56, No. 19, 1007–1010, 2020.
35. Bagaria, H. and D. Johnson, "Transient solution to the bioheat equation and optimization for magnetic fluid hyperthermia treatment," *International Journal of Hyperthermia*, Vol. 21, No. 1, 57–75, 2005.
36. Rodrigues, D., P. Pereira, P. Limão-Vieira, P. Stauffer, and P. F. Maccarini, "Study of the one dimensional and transient bioheat transfer equation: multilayer solution development and applications," *International Journal of Heat and Mass Transfer*, Vol. 62, 153–162, 2013.
37. Sharma, A., G. Dua, V. Arora, N. Kumar, and R. Mulaveesala, "A novel analytical approach for nondestructive testing and evaluation of bone implants using frequency modulated thermal wave imaging," *Lecture Notes in Mechanical Engineering*, ed, 273–285, 2022.
38. Ramp, H. O. and E. R. Wingrove, "Principles of pulse compression," *IRE Transactions on Military Electronics*, Vol. 5, No. 2, 109–116, 1961.
39. Cook, C. E. and J. Paolillo, "A pulse compression predistortion function for efficient sidelobe reduction in a high-power radar," *Proceedings of the IEEE*, Vol. 52, No. 4, 377–389, 1964.
40. Mulaveesala, R., V. J. Somayajulu, and S. Pushpraj, "Pulse compression approach to infrared nondestructive characterization," *Review of Scientific Instruments*, Vol. 79, No. 9, Art. No. 094901, 2008.
41. Mulaveesala, R., J. S. Vaddi, and P. Singh, "Pulse compression approach to infrared nondestructive characterization," *Review of Scientific Instruments*, Vol. 79, No. 9, 094901, 2008.
42. Sharma, A., G. Dua, and R. Mulaveesala, "Breast cancer detection using frequency modulated thermal wave imaging," *Imaging Science Journal*, Vol. 67, No. 7, 396–406, 2019.
43. Werner, J. and M. Buse, "Temperature profiles with respect to inhomogeneity and geometry of the human body," *Journal of Applied Physiology*, Vol. 65, No. 3, 1110–1118, 1988.
44. Williams, L. and R. Leggett, "Reference values for resting blood flow to organs of man," *Clinical Physics and Physiological Measurement*, Vol. 10, No. 3, 187, 1989.
45. González, F. J., "Noninvasive estimation of the metabolic heat production of breast tumors using digital infrared imaging," *Quantitative InfraRed Thermography Journal*, Vol. 8, No. 2, 139–148, 2011.